# Three-dimensional $T_1$ mapping demonstrates the transfer of oxygen into cerebrospinal fluid during hyperoxia

Emma Biondetti[1,2], Davide Di Censo[1,2], Sara Pomante[1,2], Stefano Censi[1,2], Ekaterina Bliakharskaia[1,2], Manuela Carriero[1,2], Francesca Graziano[1,2], Alessandra Stella Caporale[1,2], Antonio Maria Chiarelli[1,2], and Richard Geoffrey Wise[1,2]

[1]Department of Neurosciences, Imaging and Clinical Sciences, University "G. D'Annunzio" of Chieti-Pescara, Italy, Chieti, Italy

[2]Institute for Advanced Biomedical Technologies, University "G. D'Annunzio" of Chieti-Pescara, Italy, Chieti, Italy

**Corresponding author:**
Emma Biondetti, PhD
Department of Neurosciences, Imaging and Clinical Sciences
Institute for Advanced Biomedical Technologies
University “G. D’Annunzio” of Chieti-Pescara
Via dei Vestini, 31 – 66100 Chieti – Italy
E-mail: emma.biondetti@unich.it

**Abstract** (max 194/200 words)

This study developed a non-invasive magnetic resonance imaging technique to investigate the transfer of oxygen into cerebrospinal fluid (CSF) in healthy subjects. Alterations in CSF $T_1$ (longitudinal relaxation time) were induced by 100% hyperoxia and measured using a 3D SPACE sequence at 3T in 20 subjects, thereby demonstrating oxygen diffusion from blood to CSF. $T_1$ mapping was performed at high resolution (0.9-mm isotropic) to capture anatomical details of the CSF spaces and was also repeated more rapidly at a lower resolution (3-mm isotropic) to capture the temporal dynamics of $T_1$ changes. Region-dependent reductions in $T_1$ were observed, indicating increased oxygen concentration. These occurred most prominently and rapidly in the cortical subarachnoid space, stabilising within approximately 7 minutes of initiating hyperoxia, suggesting that oxygen diffusion primarily occurs via pial arteries. Slower changes, commencing after approximately 10 minutes, occurred in the posterior lateral ventricles, where choroid plexus is found. In addition to providing insights into the structure of CSF and dynamics of blood-CSF oxygen exchange, this methodology could, in the future, offer a valuable tool for characterising the passive diffusion (oxygen permeability) properties of cerebral blood vessel walls, thereby providing a potential marker of cerebrovascular integrity.

**Word count**: 5784/6000 (Abstract + Body of article + Acknowledgements)

# 1 Introduction

There is growing interest in the magnetic resonance imaging (MRI) community in developing techniques to characterise the exchange dynamics between blood, cerebrospinal fluid (CSF) and the adjacent brain parenchyma, and to understand how these processes are regulated by the blood-brain barrier (BBB) and blood-CSF barrier (BCSFB).[1] Ultimately, the efficiency of these exchange mechanisms is considered essential for removing cerebral waste products, and alterations in permeability may reveal pathological modifications to these barriers.

In this context, practical methods are needed to investigate exchange dynamics between tissue compartments. Some studies on human patient populations have administered gadolinium-based contrast agents (GBCAs) either intrathecally[2–4] or intravenously[5–7] to characterise the time course of compartmental contrast enhancement. Intrathecal GBCA injection reveals the natural exit routes in the brain clearance system, whereas intravenous injection provides information on both entry and exit pathways. Intrathecally-injected GBCA caused enhancement observable on $T_1$-weighted images within 20 minutes at the base of the skull (foramen magnum), within hours in the cortical sulci and cisternal spaces, and after 24 to 48 hours in brain tissue.[2–4] Intravenously-injected GBCA caused enhancement on $T_2$-weighted fluid-attenuated inversion recovery (FLAIR) images with a different time course, as leakage into various CSF-filled regions started hours after injection.[5–7] However, these studies were conducted in clinical cohorts and cannot be replicated in non-symptomatic individuals, due to the invasiveness of GBCA injections.[8]

Non-invasive techniques for CSF imaging have also been developed based on the transfer of water or molecular oxygen ($O_2$) between tissue compartments. CSF production is thought to primarily occur in the cerebral ventricles at the BCSFB through the exchange of water and ions from the blood in the choroid plexuses.[1] To investigate the transfer of water from blood to CSF, one study has used arterial spin labelling with a long labelling duration and post-labelling delay, showing that labelled water reaches CSF from blood within seconds.[9] According to the two traditional models for brain fluid dynamics, namely the Glymphatic System and the Intramural Peri-Arterial Drainage model (IPAD), water influx from the CSF into brain tissue occurs through specialised perivascular spaces and is driven by pulsatility of the arterial wall.[1] To investigate the transfer of water between CSF and brain parenchyma, one study has proposed an inversion-recovery approach with a long echo time (TE)[10] to measure the longitudinal relaxation time ($T_1$) of CSF, reporting that shorter $T_1$ in some regions could indicate faster CSF-brain tissue exchange.[10]

Similarly to water, which passes through the BBB and BCSFB facilitated by aquaporin water channels and co-transporters, $O_2$ can pass through the BBB and the BCSFB due to its lipid solubility and the high vascular permeability of vessels to $O_2$ (particularly in the choroid plexus and pial vessels) in proximity to CSF.[11] This transport is ultimately driven by the large concentration gradient of $O_2$ (a difference in oxygen partial pressure, $\Delta PO_2$) from the $O_2$-rich arterial blood to CSF and tissue, and will depend on the vascular permeability to $O_2$.[11] Two studies have used custom inversion-recovery sequences to map the $T_1$ of CSF before and after 100% hyperoxia and thereby map changes in the partial pressure of $O_2$.[12,13] These studies have shown regional shortening of CSF $T_1$ upon $O_2$ breathing and reported hyperoxia-induced effects in the CSF within minutes of $O_2$ administration, demonstrating the transfer of $O_2$ from the blood to the CSF compartment.[12,13] However, previous research was limited by its reliance on imaging protocols with relatively large voxel sizes or thick imaging slabs. This limitation was primarily due to the significant specific absorption rates inherent to the employed spin-echo readout techniques.

Here, we aimed to demonstrate non-invasively, with whole-brain coverage and sub-millimetric voxel resolution, the transfer of $O_2$ between the arterial blood and CSF compartments in a healthy population. To obtain suitable MRI images, we measured $T_1$ in the CSF using a tailored three-dimensional (3D) Sampling Perfection with Application-optimised Contrasts using different flip angle Evolution (SPACE) pulse sequence with a long TE that effectively suppresses signal from tissues other than CSF given the considerably longer T2 of CSF than other tissues. To obtain information on the rate of $O_2$ exchange between blood and CSF, we assessed changes in the CSF $T_1$ during the transition from room air breathing (normoxia) to hyperoxia (100% $O_2$ administration).

# 2 Subjects and methods

## 2.1 Participants

MRI data were acquired in 20 healthy subjects (10/10 males/females, average age ± standard deviation (SD): 34.5 ± 8.8 years, age range: 24-52 years). All participants reported no diagnosis of neurological, cardiovascular or respiratory conditions. This study was approved by the Institutional Review Board of the Department of Neurosciences, Imaging and Clinical Sciences, University of Chieti-Pescara (protocol number: 07/2023). All participants provided written informed consent and were instructed to abstain from consuming caffeinated or alcoholic beverages from the night before the experiment. This

research was conducted in accordance with the World Medical Association Declaration of Helsinki.

## 2.2 Experimental protocol

Before undergoing MRI, subjects were fitted with a breathing circuit as described in Tancredi et al[14] for $O_2$ delivery. The mask was secured to the subject's head using a four-point silicone harness. In the absence of a medical $O_2$ supply, the circuit provides room air to the participant. When the $O_2$ supply is switched on, the presence of a reservoir ensures that the inspired $O_2$ concentration remains consistently close to 100% even when the inspired gas flow during peak inspiration temporarily exceeds the $O_2$ source supply rate. The air composition inside the mask was monitored through a line connected to a Luer lock sampling port, which directed the samples outside the scanner room to a respiratory gas analyser (ML206, ADInstruments, Dunedin, New Zealand) connected to a PowerLab 16/35 data acquisition and analysis system (PL3516, ADInstruments). Samples were visualised and recorded using LabChart software (v8.1 Pro, ADInstruments). The subject's heartbeat and $O_2$ saturation levels were continuously monitored using a wireless pulse oximeter (Expression MR200, Philips Healthcare, Best, The Netherlands).

All subjects underwent MRI on a 3 T Prisma system using a 32-channel receive-only head coil (Siemens Healthineers, Forchheim, Germany). At the beginning of the imaging session (Figure 1), structural images were acquired for anatomical reference using an MP2RAGE sequence[15] with the following parameters: sagittal slice orientation, phase encoding direction=anterior-posterior, resolution=1-mm isotropic, field of view (foot-head x anterior-posterior x right-left)=256x256x176 $mm^3$, repetition time (TR)=5000 ms, TE=3.58 ms, inversion times (TIs)=700/2500 ms, flip angles=4/5 degrees, GRAPPA acceleration factor=3, bandwidth=180 Hz/pixel and acquisition duration=4:59 min:s.

Compared to conventional fast/turbo spin echo, the SPACE readout enables high-resolution 3D spin-echo imaging with a lower specific absorption rate. It uses non-selective, short refocusing pulse trains, alongside flip angles less than 180 degrees for the refocusing radiofrequency pulses. This combination reduces echo spacing while lengthening the usable duration of the spin-echo train and, therefore, the TE.[16] Two versions of the 3D SPACE sequence were implemented, one with an isotropic resolution of 0.9 mm and the other with an isotropic resolution of 3 mm. Both employed a long effective TE to suppress signal from brain tissue compared to CSF.

The high-resolution implementation of the 3D SPACE sequence consisted of two separate acquisitions, where all parameters were kept unchanged except for the TIs, which were set

to 3000 ms ($TI_1$) and 7550 ms ($TI_2$) to measure $T_1$. The other parameters were: sagittal slice orientation, phase encoding direction=anterior-posterior, field of view (foot-head x anterior-posterior x right-left)=230x230x158 $mm^3$, 0.9-mm isotropic resolution, TR=10010 ms, $T_2$ preparation time=200 ms, TE=751 ms, turbo factor=599, flip angle=120 degrees, GRAPPA acceleration factor=2, bandwidth=888 Hz/pixel and acquisition duration=7:52 min:s.

The low-resolution 3D SPACE sequence had similar parameters as the high-resolution version, except for the following: resolution=3 mm isotropic, field of view (foot-head x anterior-posterior x right-left)=384x306x216 $mm^3$, TE=752 ms, flip angle=115 degrees, bandwidth=494 Hz/pixel, and acquisition duration=1:42 min:s.

The high-resolution sequence was employed to calculate $T_1$ maps at baseline, during room air breathing (normoxia), and at the end of the experiment during 100% $O_2$ (hyperoxia) (Figure 1). The low-resolution sequence, with the shorter acquisition time, was used to calculate three $T_1$ maps during the first phase of $O_2$ administration, providing information on the temporal dynamics of $T_1$ changes in the CSF caused by hyperoxia. The repeats of each pair of low-resolution acquisitions will be referred to as runs 1, 2 and 3 (Figure 1).

$O_2$ was administered in two phases of the experiment (Figure 1) with flow at 15 L/min and $O_2$ humidification for subject comfort. Initially, 100% $O_2$ was administered for 10 minutes. This duration has been shown to lead to maximum observable change in $T_1$ of CSF during 100% hyperoxia.[12] The acquisition of three runs enabled the calculation of $T_1$ maps to investigate dynamic changes in $T_1$. Then, $O_2$ administration was paused for approximately 6 minutes and 30 seconds. During this period, a sequence unrelated to the present study was conducted. This pause was inserted to adhere to local safety guidelines regarding 100% $O_2$ administration. Afterwards, 100% $O_2$ administration was resumed until the end of the experiment as shown in Figure 1. The effects of hyperoxia on CSF were expected to return to the pre-pause level within the duration of the second acquisition of the high-resolution SPACE $TI_1$ sequence (Figure 1).[12]

## 2.3 High-resolution SPACE processing

Image analysis was performed using MATLAB (R2022b, The MathWorks, Natick, MA), the FMRIB software library (FSL) v6.0[17], and the Advanced Normalisation Tools (ANTs) software library.[18] In particular, all rigid image coregistrations were performed using FSL FLIRT[19,20], whereas non-linear coregistrations to standard space were performed using the ANTs SyN function.

To enable the calculation of $T_1$ maps for both pairs of high-resolution SPACE acquisitions (Figure 1), the $TI_2$ image was rigidly coregistered to the $TI_1$ image. Moreover, to ensure image alignment between normoxia and hyperoxia, the high-resolution $TI_1$ image acquired during hyperoxia was rigidly coregistered to the high-resolution $TI_1$ image acquired during normoxia (Figure 1).

A mask of CSF was calculated based on the difference between the $TI_2$ and $TI_1$ images acquired during hyperoxia, thereby exploiting the higher signal-to-noise ratio resulting from breathing 100% $O_2$ compared to breathing room air. To remove any residual tissue signal, the difference between $TI_2$ and $TI_1$ was empirically thresholded at 50% of its robust range, that is, the intensity distribution with outlier values removed, and then binarised. MATLAB's *regionprops* function was applied to select the largest connected component from the binary mask. The resulting CSF mask was then rigidly transformed into the space of the high-resolution $TI_1$ image acquired at normoxia by applying the transformation calculated earlier between $TI_1$ images at normoxia and hyperoxia.

For both pairs of high-resolution acquisitions (Figure 1), $T_1$ values were calculated within the CSF mask using qMRLab for Matlab[21] and the *inversion_recovery* routine. The general form of the longitudinal signal recovery model was used, which fits inversion recovery data (S) according to:

$$S(TI) = c\left(1 - 2\exp\left(-\frac{TI}{T_1}\right) + \exp\left(-\frac{TR}{T_1}\right)\right) \#(1)$$

where c is a constant, and the effective TIs were obtained by adding the $T_2$ preparation time to $TI_1$ and $TI_2$.

## 2.4 Low-resolution SPACE processing

Similar to Section 2.3, to enable $T_1$ calculation at each run during hyperoxia, each low-resolution $TI_2$ image was rigidly registered to the corresponding $TI_1$ image (Figure 1). For each run of the low-resolution sequence, the CSF mask for $T_1$ mapping was obtained by rigidly aligning the high-resolution $TI_1$ image acquired during hyperoxia with the low-resolution $TI_1$ image at each run, and applying the resulting transformation to the CSF mask calculated in Section 2.3. Then, for each run, $T_1$ values were calculated within the CSF mask according to Equation 1.

## 2.5 $T_1$ map alignment and difference image calculation

For visual inspection of $T_1$ alterations induced by hyperoxia, the high-resolution $T_1$ maps calculated at hyperoxia and normoxia were rigidly aligned based on the transformation

between the respective $TI_1$ images calculated earlier. Similarly, for visual inspection of the dynamic effect of $O_2$ inhalation on $T_1$, all low-resolution $T_1$ maps were aligned in the space of run 1 by calculating the rigid transformations between the $TI_1$ images from runs 2 and 3 and the $TI_1$ image from run 1, and applying the resulting transformations to the corresponding $T_1$ maps. Then, difference images were computed between the high-resolution $T_1$ maps obtained at normoxia and hyperoxia, and between each pair of low-resolution $T_1$ maps.

## 2.6 Regional analysis of $T_1$ values

For regional analysis of $T_1$ values in the CSF, the following regions of interest (ROIs) were manually delineated using ITK-SNAP within the contours of the high-resolution CSF mask: the anterior lateral ventricles (anterior to the foramen of Monro), the posterior lateral ventricles (posterior to the foramen of Monro, including the body, atrium, occipital and temporal horns of the lateral ventricles), the third ventricle (inferior to the foramen of Monro and superior to the cerebral aqueduct) and the cortical subarachnoid space. These ROIs were selected to enable comparison with previous studies investigating the $T_1$ values of CSF during hyperoxia[12] and a study suggesting that a faster CSF-tissue exchange rate characterises regions with lower $T_1$ values.[10] For each subject and all high-resolution and low-resolution $T_1$ maps, the median $T_1$ value was calculated in each ROI.

Statistical analyses of the regional median values of $T_1$ were performed using JASP (v0.19.3.0).[22] All statistical tests were two-tailed, and $p<0.05$ was considered to determine significance.

A two-way repeated-measures ANOVA was performed to test for differences in regional $T_1$ values over time based on the low-resolution SPACE data acquired during hyperoxia. Two repeated-measures factors were set: time of acquisition (runs 1 to 3) and ROI. To account for potential differences in CSF clearance influenced by the age and sex of the participants,[23,24] age was included as a covariate and sex as a between-subjects factor.

Another two-way repeated-measures ANOVA was performed to test for differences in regional $T_1$ values over time across normoxia and hyperoxia conditions based on the high-resolution SPACE data. Two repeated-measures factors were set: time of acquisition (normoxia or hyperoxia) and ROI. Similar to the previous test, participant age was included as a covariate and sex as a between-subjects factor.

For both repeated-measures ANOVA tests, assumptions were checked as follows: Mauchly's test evaluated sphericity for factors with more than two levels, Q-Q plots visually assessed

normality, and Levene's test evaluated homogeneity of variances. All post hoc analyses were performed using Holm correction to adjust *p*-values for multiple comparisons.

## 2.7 Analysis in standard space

Higher-level analysis of $T_1$ differences between normoxia and hyperoxia was performed to identify $O_2$-induced $T_1$ shortening at the group level. To this aim, for each subject, both the high-resolution $T_1$ maps calculated at normoxia and hyperoxia were registered to the 1-mm isotropic Montreal Neurological Institute (MNI) template as follows.

First, the $TI_1$ image of each SPACE acquisition was rigidly aligned to the structural $T_1$-weighted MP2RAGE uniform (UNI) image. Compared to conventional $T_1$-weighted sequences at 3 T, the MP2RAGE UNI image is designed to provide uniform intensity across the scanned volume by correcting for non-$T_1$ contrast effects, such as receiver field ($B_1$) inhomogeneity, proton density contrast and transverse decay ($T_2$*).[15] Moreover, it presents no signal in the CSF, thereby providing a contrast complementary to that observed in the SPACE acquisitions. To enable more accurate registration, strong background noise in air-filled regions was removed from the MP2RAGE UNI image using a MATLAB implementation (*RobustCombination.m* function, https://github.com/JosePMarques/MP2RAGE-related-scripts) of the method proposed by O'Brien and colleagues.[25] This denoised image was used as input for an optimised atlas-based brain extraction algorithm based on ANTs. The extracted brain region was then coregistered to the 1-mm isotropic MNI template using ANTs. The same image transformation was applied to align the individual high-resolution $T_1$ maps to MNI space.

Using a custom implementation of nearest-neighbour interpolation in MATLAB, each $T_1$ map in MNI space was downsampled to an isotropic 3-mm resolution. This downsampled voxel size was chosen to reduce the impact of slight misalignment between individual $T_1$ maps in MNI space and improve the statistical power of group-level analysis. Because the $T_1$ maps of CSF were sparse in nature, with NaN values assigned to voxels with no CSF signal, the custom implementation of nearest-neighbour interpolation explicitly checked for NaN values at the nearest-neighbour location. If a NaN value was found, the algorithm searched a 3x3x3 neighbourhood for the closest non-NaN value to fill the gap in the downsampled image.

The average $T_1$ maps at normoxia and hyperoxia were calculated across subjects. To account for data sparsity, the average $T_1$ value of a voxel was only calculated if the voxel had a value different from NaN in at least 90% of subjects. Otherwise, the average of $T_1$ in that voxel was set to zero. To assess differences in $T_1$ of CSF between normoxia and hyperoxia, non-parametric permutation tests were conducted using the *randomise* tool in

FSL.[26] Two distinct one-tailed one-sample t-tests were performed to test for $\Delta T_1 > 0$ and $\Delta T_1 < 0$ (where $\Delta$ denotes a difference) by providing as input a series of difference images (one per subject) between the $T_1$ map calculated at normoxia and the $T_1$ map calculated at hyperoxia. To maintain the family-wise error rate at 0.05, a threshold of $p<0.025$ was used for each of these two tests (Bonferroni correction). The binary CSF mask for the tests was calculated to include the voxels appearing in both the average $T_1$ maps at normoxia and hyperoxia. For each test, 5000 permutations were used, along with the bi-dimensional version of threshold-free cluster enhancement, which is designed to correct for multiple comparisons when using sparse images.

# 3 Results

## 3.1 Overall CSF appearance on SPACE acquisitions

Figure 2 shows images acquired using the high-resolution SPACE sequence (Figures 2a-b) and the low-resolution SPACE sequence (Figures 2c-d) at the two TIs. Lower windowing was applied to the images at the shorter TI, where CSF was nearly null (Figures 2a and 2c). Notably, residual non-CSF signal appeared only outside the brain, suggesting that the chosen TE effectively minimised signal contributions from brain parenchyma (Figure 2).

## 3.2 $T_1$ mapping

Figure 3 shows representative high-resolution $T_1$ maps acquired at normoxia (Figure 3a) and hyperoxia (Figure 3b). It also shows the difference between these two maps (Figure 3c) and the ROIs used for regional analysis of $T_1$ (Figure 3d). Compared to breathing room air, $O_2$ inhalation caused widespread $T_1$ shortening in the cortical subarachnoid space (Figures 3a-c).

## 3.3 Regional analysis of $T_1$

The regional values of $T_1$ are shown using raincloud plots for both the high-resolution (Figure 5) and low-resolution SPACE acquisitions (Figure 6).

In both repeated measures ANOVA tests, Mauchly's test of sphericity was significant, so the Greenhouse-Geisser correction was applied. The assumptions of normality and variance homogeneity were satisfied.

### 3.3.1 Regional high-resolution $T_1$ measurements

There was a significant main effect of ROI on $T_1$ of CSF, $F(1.893, 32.173)=18.009$, $p<0.001$, $\omega^2=0.250$. Moreover, the effect of hyperoxia on $T_1$ was ROI-dependent, $F(1.786, 30.360)=8.646$, $p=0.001$, $\omega^2=0.034$. Finally, there was a marginal between-subjects effect of age on $T_1$, $F(1, 17)=3.811$, $p=0.068$, $\omega^2=0.072$.

The post-hoc tests revealed the following. Overall, there was a significant decrease in $T_1$ of CSF during hyperoxia compared to normoxia (mean difference=80.2 ms, $p<0.001$). Moreover, CSF $T_1$ in the anterior lateral ventricles was significantly higher than in all other ROIs: the posterior lateral ventricles (mean difference=118.0 s, $p<0.001$), the third ventricle (mean difference=204.6 ms, $p<0.001$) and the subarachnoid space (mean difference=505.9 ms, $p<0.001$). CSF $T_1$ was significantly higher in the posterior lateral ventricles than in both the third ventricle (mean difference=86.6 ms, $p<0.001$) and cortical subarachnoid space (mean difference=387.8 ms, $p<0.001$), and CSF $T_1$ was significantly higher in the third ventricle than in the cortical subarachnoid space (mean difference=301.2 ms, $p<0.001$). On a regional basis, hyperoxia caused a significant decrease in CSF $T_1$ in the posterior lateral ventricles ($p=0.008$, Figure 5b) and, more markedly, in the cortical subarachnoid space ($p<0.001$, Figure 5d), but not in the other ROIs (Figure 5a and 5c).

### 3.3.2 Regional low-resolution $T_1$ measurements

There was a significant main effect of ROI on $T_1$ of CSF, $F(1.910, 32.5)=12.018$, $p<0.001$, $\omega^2=0.169$. The between-subject effect of age on $T_1$ was also significant, $F(1, 17)=6.634$, $p=0.02$, $\omega^2=0.135$. Finally, there was a marginally significant main effect of time on $T_1$, $F(1.601, 27.2)=2.969$, $p=0.08$, $\omega^2=0.018$. While not reaching statistical significance, the *p*-value=0.08 suggested a trend towards differences in $T_1$ across runs.

Post-hoc tests using the Holm correction revealed the following. Overall, there was a significant decrease in $T_1$ of CSF between runs 1 and 3 (mean difference=87.8 ms, $p<0.001$). Moreover, CSF $T_1$ in the anterior lateral ventricles was significantly higher than in all other ROIs: the posterior lateral ventricles (mean difference=200.5 ms, $p<0.001$), the third ventricle (mean difference=267.5 ms, $p<0.001$) and the subarachnoid space (mean difference=669.2 ms, $p<0.001$). Similarly, both the posterior lateral ventricles (mean difference=468.7 ms, $p<0.001$) and the third ventricle (mean difference=401.8 ms, $p<0.001$) had a significantly higher $T_1$ than the one measured in the cortical subarachnoid space. Finally, post hoc tests on the interaction between ROI and time revealed that, in the posterior lateral ventricles, $T_1$ decreased significantly between runs 1 and 3 (mean difference=70.0 ms, $p=0.03$) and, in the cortical subarachnoid space, $T_1$ decreased significantly between

runs 1 and 2 (mean difference=181.1 ms, $p<0.001$) and between runs 1 and 3 (mean difference=231.9 ms, $p<0.001$). On a regional basis, CSF $T_1$ significantly decreased between runs 1 and 3 in the posterior lateral ventricles ($p=0.025$, Figure 6b) and between runs 1 and 2 ($p<0.001$) and 1 and 3 ($p<0.001$) in the cortical subarachnoid space (Figure 6d).

### 3.4 Higher-level analysis of $T_1$

Figure 7 displays, in MNI space, the across-subject average of the high-resolution $T_1$ maps of CSF acquired during normoxia (Figure 7a) and hyperoxia (Figure 7b), along with the $T_1$ difference map between these two conditions (Figure 7c) and the (1 - *p*) voxel-wise statistical map resulting from the permutation test assessing higher $T_1$ values at normoxia than hyperoxia (Figure 7d). Results from the permutation test assessing lower $T_1$ values at normoxia than hyperoxia are not shown, as no significant differences were found. The group-level analysis revealed significant $T_1$ shortening widespread across the cortical subarachnoid space and, to a lesser degree, in posterior ventricular regions (Figure 7d). $T_1$ values appeared unchanged in the anterior ventricles (Figure 7d).

## 4 Discussion

Using a customised whole-brain SPACE MRI protocol, with a long TE to minimise contributions from brain parenchyma, and a hyperoxia protocol, this study examined how 100% $O_2$ inhalation affects the $T_1$ of CSF across the whole brain in healthy participants. High-resolution and low-resolution acquisitions, with a long TE, enabled the calculation of 3D $T_1$ maps of brain CSF, free from signal contamination from surrounding brain tissue. These maps revealed that $O_2$ inhalation causes widespread $T_1$ shortening in the cortical subarachnoid space, but not in all ventricular regions over the 10-15 minute timescale of hypoxia studied here. Furthermore, in the cortical subarachnoid space, $O_2$-induced $T_1$ shortening of CSF stabilised after approximately 7 minutes of continuous $O_2$ breathing (Figure 6d).

In the present study, the SPACE sequence[16] was specifically optimised to provide 3D acquisitions with sub-millimetric resolution, making it suitable for studying CSF anatomy. Previous studies on hydrocephalus[27,28] have proposed a similar adaptation of the SPACE protocol to illustrate CSF anatomy, but the present study is the first to propose the SPACE protocol for $T_1$ mapping in this area. The SPACE sequence was also modified to achieve a faster acquisition time by lowering the image resolution, enabling the observation of time-dependent CSF $T_1$ changes during hyperoxia. The present application of the SPACE

sequence represents a flexible tool that can be adapted in future studies, with a focus on the structural aspects of CSF anatomy or the dynamic changes in CSF longitudinal relaxation time constant. While tested on a Siemens system, protocols from other MRI manufacturers offer potential for similar modifications: the Volume ISotropic Turbo spin echo Acquisition (VISTA) (Philips Healthcare, Best, The Netherlands) and the CUBE sequence (GE Healthcare, IL, USA).

Having such a protocol readily available on clinical MR systems is timely, given the growing interest in cerebral CSF spaces and CSF circulation.[29] One limitation of the proposed protocol is its long duration for high-resolution $T_1$ mapping (approximately 15 minutes). However, considering that basic science research is a primary focus of the neurofluids field, we believe that such a long acquisition time in a research setting on healthy subjects is manageable. Future work exploring specific clinical applications of this protocol could refine it for targeted clinical questions within more acceptable examination times.

Regional analysis of $T_1$ in CSF-containing structures showed that, at baseline, the median $T_1$ of CSF was systematically longer in the anterior lateral ventricles compared to all other regions (Figure 5, normoxia, and Section 3.3.1). This result agrees with a previous study showing that CSF in the frontal horns of the lateral ventricles has baseline $T_1$ values significantly longer than in the subarachnoid space. This observation may be caused by the lack of blood-CSF water exchange sites in the anterior ventricles.[10] The presence of such sites elsewhere, specifically the choroid plexuses in the ventricles or pial arteries entering the brain from the subarachnoid space, allows for transfer of water from blood, having a relatively short $T_1$,[30] to CSF. This mixing effectively shortens the $T_1$ of CSF relative to areas without blood-CSF water exchange.

In the cortical subarachnoid space, 100% hyperoxia significantly reduced $T_1$ compared to baseline values (Figure 5d) over a timescale of minutes (Figure 6d). In this ROI, the observed $T_1$ shortening at our chosen timescale was consistent with previous studies applying a 100% hyperoxic challenge for 15 or 30 minutes.[12,31] Additionally, the rapid hyperoxia-induced $T_1$ shortening in sulcal CSF was consistent with a study reporting a dynamic signal increase on fast/turbo spin echo images during 5 minutes of 100% hyperoxia.[32] However, previous studies reported no $T_1$ change in the lateral ventricles during 100% hyperoxia.[12,31,32] Here, instead, $T_1$ was reduced in the posterior lateral ventricles compared to baseline values (Figure 5b), but the change occurred over a longer timescale than in the cortical subarachnoid space (Figure 6b). Differences in observations across studies might be due to varying definitions of ROIs within the lateral ventricles. One study segmented a region in the anterior horns of the lateral ventricles based on a 20-mm-thick

oblique coronal 3D slab,[12] while the others segmented a region across the entire lateral ventricles based on a 91.5-mm-thick transverse 3D slab[31] or a single 7-mm-thick transverse 2D slice.[32] In contrast, the present study subdivided the lateral ventricles into anterior and posterior, highlighting that $T_1$ shortening related to 100% hyperoxia only occurs over the timescales studied here in the medial-posterior part of the lateral ventricles, where the choroid plexuses are located. Stable $T_1$ values in the third ventricle during 100% hyperoxia were consistent with previous results,[12] but seem inconsistent with the anatomy of this region, which contains choroid plexuses along its roof, connected with those in the lateral ventricles through the interventricular foramina (of Monro). The timescale selected in this and earlier studies may have been insufficient to detect $T_1$ shortening throughout all large-volume CSF compartments.

During 100% hyperoxia, the larger and faster change in $T_1$ in the cortical subarachnoid space compared to the posterior ventricular regions (Figures 5b, 5d, 6b and 6d) is likely to be related to the nature of blood-CSF exchange sites and the volume of CSF present in each compartment. These two factors are discussed in more detail below.

Around the cortex, $O_2$ from blood enters the CSF via pial arteries on the brain surface, which are part of a network within the subarachnoid space, a CSF-filled space located between the pia mater and arachnoid mater. Pial arteries have thick walls composed of endothelium, basement membranes and layers of smooth muscle.[33] Because, unlike parenchymal arteries and capillaries, pial arteries are directly adjacent to the CSF, a difference of oxygen partial pressure ($\Delta PO_2$) exists that favours passive outward diffusion of $O_2$ into CSF. This diffusion, sometimes termed pre-capillary $O_2$ shunting, allows $O_2$ to enter the CSF before the blood reaches the capillaries.[34] In the ventricles, $O_2$ from blood enters the CSF via the choroid plexus, a highly vascularised structure composed of villi, each containing fenestrated capillaries, stromal tissue, and a layer of choroidal epithelial cells interconnected by tight junctions, which form the BCSFB.[35] $O_2$ dissolved in plasma is expected to diffuse rapidly and freely across these structures.[35,36]

We suggest that a key factor determining the rate and degree of $T_1$ shortening in a given CSF compartment is the relationship between the permeability surface area product of the local BCSFB and the volume of CSF into which $O_2$ is transferred. We hypothesise that there is a greater ratio of pial arteries relative to the sulcal CSF volume than there is of choroid plexus vessels relative to ventricular CSF volume, thereby resulting in a faster and greater $T_1$ shortening in the cortical subarachnoid space during hyperoxia.[31] In ventricular CSF, the dilution of $O_2$, related to the local volume of CSF, is likely to be slower compared to sulcal CSF. This explanation has also been proposed by studies performed in subjects receiving

100% $O_2$ under general anaesthesia[37] or through a face mask,[38] which showed signal hyperintensities in subarachnoid CSF much higher than in ventricular CSF on fluid-attenuated inversion recovery MRI.[37,38]

In addition to the number of vessels exchanging $O_2$, their permeability surface area product will depend on the structure of the vascular walls and thus their permeability. We propose that another factor influencing $O_2$ transfer from blood into ventricular CSF is $O_2$ consumption within the BCSFB structure. In pial arteries, $O_2$ diffuses relatively freely along a steep driving $\Delta PO_2$. In contrast, at the choroid plexus-CSF interface, epithelial cells are highly active in CSF secretion (via ion pumping) and are rich in mitochondria to support this process.[39] We hypothesise that this high metabolic activity makes the epithelium a metabolic sink, rapidly consuming $O_2$ that diffuses into the stroma. Consequently, the final $\Delta PO_2$ driving $O_2$ into the bulk ventricular CSF is reduced due to this consumption, making the transfer rate different from that in the pial artery wall. Furthermore, differences in the baseline $PO_2$ within the ventricles and the sulci, driven in part by the continuous circulation and bulk flow of CSF, may also contribute to the local $\Delta PO_2$ and the effective volume of $O_2$ distribution.

Based on our observations, we propose that $O_2$ delivered via hyperoxia may be better suited for investigating exchange between blood and CSF compartments compared to GBCAs. Firstly, $O_2$ is a simple, rapidly metabolised molecule that avoids the risks of synthetic pharmaceuticals like GBCAs. Secondly, the two compounds differ in their transport mechanisms: $O_2$ is a small, uncharged, highly lipophilic gas that rapidly traverses endothelial cell lipid membranes via passive diffusion, reflecting transmembrane permeability. GBCAs, conversely, are significantly larger, polar, hydrophilic molecules with a restricted, slower exchange primarily limited by paracellular transport through tight junctions between endothelial cells.[5–7] Therefore, $O_2$ could probe transmembrane exchange, whereas GBCAs probe the size-exclusion properties of tight junctions. Thus, in the future, $T_1$ shortening related to the $O_2$ transfer rate from pial arteries to CSF (or penetrating arteries and the adjacent perivascular spaces or brain tissue) could serve as a marker of the vessel wall's effective permeability to $O_2$, and by extension, its passive diffusion properties for other small, lipid-soluble molecules. Indeed, we expect the rate of $O_2$ loss to be proportional to the permeability-surface area product of the vessel wall, which represents its effective "leakiness" to $O_2$. Thus, for a given $\Delta PO_2$, a higher $O_2$ transfer rate implies a higher effective $O_2$ permeability. Factors that alter the physical structure of the arterial wall, such as the number of cell layers, cell junction tightness, or the thickness of the barrier, will affect $O_2$ movement. Therefore, a change in the $O_2$ transfer rate could correlate with a change in the passive permeability coefficient for other small, passively diffusing molecules, potentially

establishing $O_2$ diffusion as a new marker of vascular structure in pathologies affecting the vasculature, such as dementia.[40] Notably, measurements of the $O_2$ transfer rate from pial or penetrating arterioles will only reflect the permeability of the arteriolar wall, which is structurally different from the BBB located at the capillaries.

Potential limitations should be considered when interpreting these results. One factor influencing $T_1$ shortening in the cortical subarachnoid space compared to the ventricles could be partial voluming with the surrounding brain parenchyma, which is $T_1$-insensitive to hyperoxia,[31] and may dilute hyperoxia-induced $T_1$ changes in CSF. However, this was addressed by using an extralong TE value to suppress signals from the brain parenchyma around CSF-containing structures (Figure 2), making it unlikely that partial voluming significantly affected the measured $T_1$. Furthermore, the influence of hyperoxia on CSF hydrodynamics warrants consideration. Although the effects of normobaric 100% hyperoxia on CSF dynamics in healthy controls have not been investigated, in traumatic brain injury patients, short-term (2 hours) normobaric 100% hyperoxia significantly increased local brain tissue oxygenation without affecting intracranial pressure, cerebral perfusion pressure, or mean arterial pressure.[41] Thus, our sub-30-minute hyperoxia exposure was unlikely to affect CSF dynamics. Notably, subjects were imaged supine, which enhances CSF flow compared to upright positions.[42,43] Consequently, the observed $T_1$ shortening during hyperoxia mainly applies to the supine position used in high-field MRI.

To conclude, this study applied a 3D sequence for imaging CSF and measuring CSF $T_1$ across the entire brain, adapting a protocol available on clinical MR systems. Experiments conducted with 100% hyperoxia demonstrated that $O_2$ induces $T_1$ shortening effects in the CSF, these occurring more rapidly in the subarachnoid space than in the ventricles. This finding is consistent with the passive diffusion of $O_2$ across the high density of blood-CSF exchange sites around the cortex. The methodology presented could help characterise CSF structures and assess vascular permeability to $O_2$, serving as a marker of cerebrovascular health.

# 5 Acknowledgements

The authors thank Darien Calvo Garcia and Daniele Petrucci for practical help with the MRI acquisitions.

# 6 Author contribution statement

**Emma Biondetti:** conceptualisation, data curation, formal analysis, funding acquisition, investigation, methodology, project administration, resources, software, visualisation, writing (original draft).

**Davide Di Censo:** data curation, formal analysis, investigation, methodology, software, writing (reviewing & editing).

**Sara Pomante**: investigation, writing (reviewing & editing).

**Stefano Censi**: investigation, methodology, writing (reviewing & editing).

**Ekaterina Bliakharskaia**: investigation, writing (reviewing & editing).

**Manuela Carriero**: writing (reviewing & editing).

**Francesca Graziano**: investigation, writing (reviewing & editing).

**Alessandra Stella Caporale**: methodology, writing (reviewing & editing).

**Antonio Maria Chiarelli:** funding acquisition, methodology, writing (reviewing & editing).

**Richard Geoffrey Wise:** funding acquisition, methodology, project administration, resources, supervision, writing (reviewing & editing).

# 7 Statements and declarations

## 7.1 Ethical considerations

This study was approved by the Institutional Review Board of the Department of Neurosciences, Imaging and Clinical Sciences, University of Chieti-Pescara (Comitato di Revisione della Ricerca sull'Essere Umano – CReREU, protocol number: 07/2023) on the 16th February 2024. This research was conducted ethically, in accordance with the World Medical Association Declaration of Helsinki.

## 7.2 Consent to participate

All participants provided written informed consent before enrolment in the study.

## 7.3 Consent for publication

All participants provided written informed consent to publish the results from this study.

## 7.4 Declaration of conflicting interest

Manuela Carriero received research support from Siemens Healthineers (Forchheim, Germany).

## 7.5 Funding statements

The authors disclosed receipt of the following financial support for the research, authorship, and/or publication of this article. Emma Biondetti was supported by the European Union (EU)'s Horizon Europe research and innovation programme under the Marie Skłodowska-Curie Grant Agreement No 101066055 (HERMES). Alessandra Stella Caporale was partially supported by the Fund for the Promotion and Development of Policies of the National Research Program, as per DM 737/2021 issued by the Italian Ministry of University and Research (MUR). The other authors were partially supported by: EU-NextGenerationEU-MUR, National Plan for Recovery and Resilience (PNRR). Project number/CUP: ECS00000041/D73C22000840006; PE0000006/B83C22004960002. EU-NextGenerationEU-MUR, Research National Program (PNR) and Projects of National Relevance (PRIN). Project number/CUP: 2022BERM2F/D53D23013410001. EUNextGenerationEU-MUR, PNRR and PRIN. Project number/CUP: P2022ESHT4/D53D23019210001; 2022MHMSSJ/D53C24004560006; P20225AEEE/D53D23021480001.

## 7.6 Data availability

The anonymised and defaced MR acquisitions supporting the findings from this study are available in this open repository: https://doi.org/10.5281/zenodo.17672757.

# 8 References

1. Agarwal N, Lewis LD, Hirschler L, et al. Current Understanding of the Anatomy, Physiology, and Magnetic Resonance Imaging of Neurofluids: Update From the 2022 " ISMRM Imaging Neurofluids Study group" Workshop in Rome. *Magnetic Resonance Imaging* 2024; 59: 431–449.

2. Ringstad G, Valnes LM, Dale AM, et al. Brain-wide glymphatic enhancement and clearance in humans assessed with MRI. *JCI Insight*; 3. Epub ahead of print 26 July 2018. DOI: 10.1172/jci.insight.121537.

3. Eide PK, Vatnehol SAS, Emblem KE, et al. Magnetic resonance imaging provides evidence of glymphatic drainage from human brain to cervical lymph nodes. *Sci Rep* 2018; 8: 7194.

4. Ringstad G, Vatnehol SAS, Eide PK. Glymphatic MRI in idiopathic normal pressure hydrocephalus. *Brain* 2017; 140: 2691–2705.

5. Ohashi T, Naganawa S, Iwata S, et al. Age-related changes in the distribution of intravenously administered gadolinium-based contrast agents leaked into the cerebrospinal fluid in patients with suspected endolymphatic hydrops. *Jpn J Radiol* 2021; 39: 433–441.

6. Naganawa S, Suzuki K, Yamazaki M, et al. Serial Scans in Healthy Volunteers Following Intravenous Administration of Gadoteridol: Time Course of Contrast Enhancement in Various Cranial Fluid Spaces. *Magnetic Resonance in Medical Sciences* 2014; 13: 7–13.

7. Naganawa S, Ito R, Nakamichi R, et al. Relationship between Parasagittal Perivenous Cysts and Leakage of Gadolinium-based Contrast Agents into the Subarachnoid Space around the Cortical Veins after Intravenous Administration. *Magn Reson Med Sci* 2021; 20: 245–252.

8. Patel M, Atyani A, Salameh J-P, et al. Safety of Intrathecal Administration of Gadolinium-based Contrast Agents: A Systematic Review and Meta-Analysis. *Radiology*. Epub ahead of print 28 July 2020. DOI: 10.1148/radiol.2020191373.

9. Petitclerc L, Hirschler L, Wells JA, et al. Ultra-long-TE arterial spin labeling reveals rapid and brain-wide blood-to-CSF water transport in humans. *NeuroImage* 2021; 245: 118755.

10. Jiang D, Gou Y, Wei Z, et al. Quantification of $T_1$ and $T_2$ of subarachnoid CSF□: Implications for water exchange between CSF and brain tissues. *Magnetic Resonance in Med* 2023; 90: 2411–2419.

11. Redzic Z. Molecular biology of the blood-brain and the blood-cerebrospinal fluid barriers: similarities and differences. *Fluids and Barriers of the CNS* 2011; 8: 3.

12. Zaharchuk G, Martin AJ, Rosenthal G, et al. Measurement of cerebrospinal fluid oxygen partial pressure in humans using MRI. *Magnetic Resonance in Medicine* 2005; 54: 113–121.

13. Zaharchuk G, Busse RF, Rosenthal G, et al. Noninvasive Oxygen Partial Pressure Measurement of Human Body Fluids In Vivo Using Magnetic Resonance Imaging. *Academic Radiology* 2006; 13: 1016–1024.

14. Tancredi FB, Lajoie I, Hoge RD. A simple breathing circuit allowing precise control of inspiratory gases for experimental respiratory manipulations. *BMC Research Notes* 2014; 7: 235.

15. Marques JP, Kober T, Krueger G, et al. MP2RAGE, a self bias-field corrected sequence for improved segmentation and T1-mapping at high field. *NeuroImage* 2010; 49: 1271–1281.

16. Mugler III JP. Optimized three-dimensional fast-spin-echo MRI. *Journal of Magnetic Resonance Imaging* 2014; 39: 745–767.

17. Jenkinson M, Beckmann CF, Behrens TEJ, et al. FSL. *Neuroimage* 2012; 62: 782–790.

18. Tustison NJ, Cook PA, Holbrook AJ, et al. The ANTsX ecosystem for quantitative biological and medical imaging. *Sci Rep* 2021; 11: 9068.

19. Jenkinson M, Bannister P, Brady M, et al. Improved optimization for the robust and accurate linear registration and motion correction of brain images. *Neuroimage* 2002; 17: 825–841.

20. Jenkinson M, Smith S. A global optimisation method for robust affine registration of brain images. *Med Image Anal* 2001; 5: 143–156.

21. Karakuzu A, Boudreau M, Duval T, et al. qMRLab: Quantitative MRI analysis, under one umbrella. *JOSS* 2020; 5: 2343.

22. JASP Team. JASP (Version 0.19.3)[Computer software], https://jasp-stats.org/ (2025).

23. Han F, Liu X, Yang Y, et al. Sex-specific age-related differences in cerebrospinal fluid clearance assessed by resting-state functional magnetic resonance imaging. *NeuroImage* 2024; 302: 120905.

24. Zhang Y, Zhang R, Ye Y, et al. The Influence of Demographics and Vascular Risk Factors on Glymphatic Function Measured by Diffusion Along Perivascular Space. *Front Aging Neurosci*; 13. Epub ahead of print 19 July 2021. DOI: 10.3389/fnagi.2021.693787.

25. O'Brien KR, Kober T, Hagmann P, et al. Robust T1-Weighted Structural Brain Imaging and Morphometry at 7T Using MP2RAGE. *PLOS ONE* 2014; 9: e99676.

26. Winkler AM, Ridgway GR, Webster MA, et al. Permutation inference for the general linear model. *NeuroImage* 2014; 92: 381–397.

27. Ucar M, Tokgoz N, Damar C, et al. Diagnostic performance of heavily T2-weighted techniques in obstructive hydrocephalus: comparison study of two different 3D heavily T2-weighted and conventional T2-weighted sequences. *Jpn J Radiol* 2015; 33: 94–101.

28. Hodel J, Silvera J, Bekaert O, et al. Intracranial cerebrospinal fluid spaces imaging using a pulse-triggered three-dimensional turbo spin echo MR sequence with variable flip-angle distribution. *Eur Radiol* 2011; 21: 402–410.

29. Agarwal N, Lewis LD, Hirschler L, et al. Current Understanding of the Anatomy, Physiology, and Magnetic Resonance Imaging of Neurofluids: Update From the 2022 "ISMRM Imaging Neurofluids Study group" Workshop in Rome. *Journal of Magnetic Resonance Imaging* 2024; 59: 431–449.

30. Lu H, Clingman C, Golay X, et al. Determining the longitudinal relaxation time (T1) of blood at 3.0 Tesla. *Magnetic Resonance in Medicine* 2004; 52: 679–682.

31. Bhogal AA, Siero JC, Zwanenburg J, et al. Quantitative T1 mapping under precisely controlled graded hyperoxia at 7T. *J Cereb Blood Flow Metab* 2017; 37: 1461–1469.

32. Mehemed TM, Fushimi Y, Okada T, et al. Dynamic Oxygen-Enhanced MRI of Cerebrospinal Fluid. *PLOS ONE* 2014; 9: e100723.

33. Agarwal N, Carare RO. Cerebral Vessels: An Overview of Anatomy, Physiology, and Role in the Drainage of Fluids and Solutes. *Front Neurol*; 11. Epub ahead of print 13 January 2021. DOI: 10.3389/fneur.2020.611485.

34. Tsai AG, Johnson PC, Intaglietta M. Oxygen Gradients in the Microcirculation. *Physiological Reviews* 2003; 83: 933–963.

35. Sun Z, Li C, Leitner D, et al. Age-related Vascular Alterations in the Choroid Plexus: Novel Insights from Pathophysiology and Imaging Studies. *Aging and disease* 2025; 0.

36. MacAulay N, Keep RF, Zeuthen T. Cerebrospinal fluid production by the choroid plexus: a century of barrier research revisited. *Fluids Barriers CNS* 2022; 19: 26.

37. Frigon C, Jardine DS, Weinberger E, et al. Fraction of Inspired Oxygen in Relation to Cerebrospinal Fluid Hyperintensity on FLAIR MR Imaging of the Brain in Children and Young Adults Undergoing Anesthesia. *American Journal of Roentgenology* 2002; 179: 791–796.

38. Braga FT, da Rocha AJ, Hernandez Filho G, et al. Relationship between the concentration of supplemental oxygen and signal intensity of CSF depicted by fluid-attenuated inversion recovery imaging. *AJNR Am J Neuroradiol* 2003; 24: 1863–1868.

39. Cornford EM, Varesi JB, Hyman S, et al. Mitochondrial content of choroid plexus epithelium. *Exp Brain Res* 1997; 116: 399–405.

40. de la Torre J. The Vascular Hypothesis of Alzheimer's Disease: A Key to Preclinical Prediction of Dementia Using Neuroimaging. *J Alzheimers Dis* 2018; 63: 35–52.

41. Puccio AM, Hoffman LA, Bayir H, et al. Effect of Short Periods of Normobaric Hyperoxia on Local Brain Tissue Oxygenation and Cerebrospinal Fluid Oxidative Stress Markers in Severe Traumatic Brain Injury. *J Neurotrauma* 2009; 26: 1241–1249.

42. Alperin N, Lee SH, Sivaramakrishnan A, et al. Quantifying the effect of posture on intracranial physiology in humans by MRI flow studies. *Journal of Magnetic Resonance Imaging* 2005; 22: 591–596.

43. Muccio M, Chu D, Minkoff L, et al. Upright versus supine MRI: effects of body position on craniocervical CSF flow. *Fluids and Barriers of the CNS* 2021; 18: 61.

# 9 Figure legends

**Figure 1. Experimental protocol.** The diagram shows the time allocated for the sequences in this study. The region shaded in light blue corresponds to 100% $O_2$ administration. The open time slots during the experiment were allocated for imaging unrelated to the present study. The labels' run 1', 'run 2' and 'run 3' denote the three pairs of low-resolution SPACE acquisitions performed during the first phase of $O_2$ administration.

**Figure 2. Representative SPACE acquisitions.** For a representative subject, the same sagittal, coronal and transverse slices are shown for the high-resolution SPACE acquisition acquired at normoxia at $TI_1$ (a) and $TI_2$ (b). Similar slices are shown for the first run of the

low-resolution SPACE acquisition at $TI_1$ (c) and $TI_2$ (d). The slices depicted in (c) and (d) were cropped to match the field of view of those in (a) and (b).

**Figure 3. High-resolution $T_1$ maps.** For the same representative subject as in Figure 2, the same sagittal, coronal and transverse slices are shown for the $T_1$ maps acquired during normoxia (a), hyperoxia (b) and the difference between the two (c). The maps in panels a-c are overlaid on the high-resolution SPACE image acquired at $TI_2$. The ROIs used for regional analysis of $T_1$ values in the CSF are shown in (d) overlaid on the high-resolution SPACE image acquired at $TI_2$ during hyperoxia.

**Figure 4. Low-resolution $T_1$ maps.** For the same representative subject as in Figure 2, the same sagittal, coronal and transverse slices are shown for the $T_1$ maps acquired during hyperoxia at run 1 (a), run 2 (b), and run 3 (c). $T_1$ difference maps between each pair of runs are shown in (d-f).

**Figure 5. Raincloud plots of regional high-resolution $T_1$ measurements.** For each ROI, the individual subject median values of $T_1$ measured during normoxia and hyperoxia are shown using a raincloud plot. This plot includes, for each experimental condition, a scatter plot of individual data points, a box plot, and a histogram. In the scatter plots for each region, pairs of data points connected by a line indicate measurements from the same subject under the two experimental conditions. Significant differences between the two experimental conditions are denoted as ** $p<0.01$, *** $p<0.001$.

**Figure 6. Raincloud plots of regional low-resolution $T_1$ measurements.** For each ROI, the individual median values of $T_1$ measured at three time points (runs 1, 2 and 3) during hyperoxia are shown using a raincloud plot. This plot includes, for each run, a scatter plot of individual data points, a box plot, and a histogram. In the scatter plots for each region, triplets of data points connected by a line indicate measurements from the same subject taken at each time point. Significant differences between the three time points are denoted as * $p<0.05$, *** $p<0.001$.

**Figure 7. Average $T_1$ maps in MNI space.** The same sagittal, coronal and transverse slices are shown for the average $T_1$ maps in MNI space acquired during normoxia (a), hyperoxia (b) and the difference between the two (c). The results of the non-parametric permutation test comparing higher $T_1$ at normoxia than hyperoxia are shown in (d). All maps are shown overlaid on the 1-mm isotropic $T_1$-weighted MNI template.

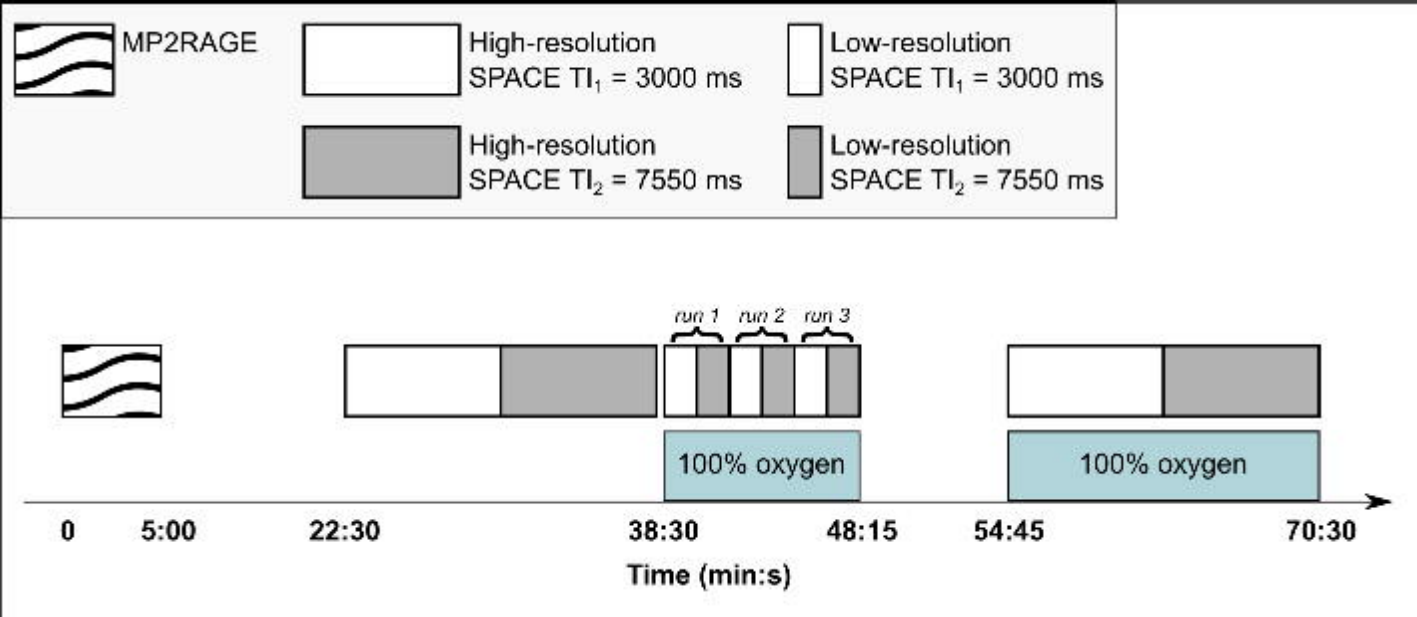
MP2RAGE
High-resolution SPACE TI1 = 3000 ms
Low-resolution SPACE TI1 = 3000 ms
High-resolution SPACE TI2 = 7550 ms
Low-resolution SPACE TI2 = 7550 ms
run 1
run 2
run 3
100% oxygen
100% oxygen
0
5:00
22:30
38:30
48:15
54:45
70:30
Time (min:s)

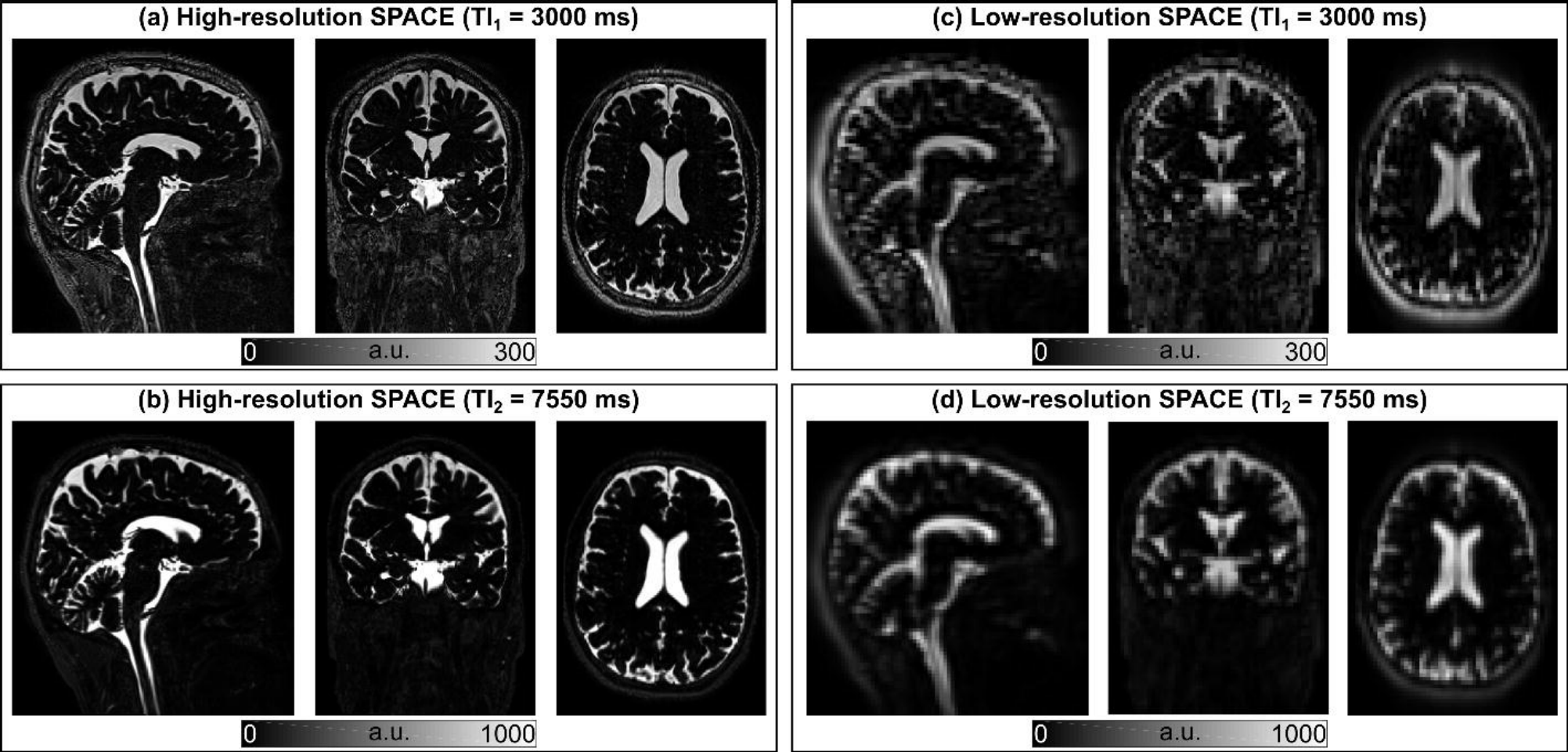
(a) High-resolution SPACE (TI1 = 3000 ms)
0
a.u.
300
(c) Low-resolution SPACE (TI1 = 3000 ms)
0
a.u.
300
(b) High-resolution SPACE (TI2 = 7550 ms)
0
a.u.
1000
(d) Low-resolution SPACE (TI2 = 7550 ms)
0
a.u.
1000

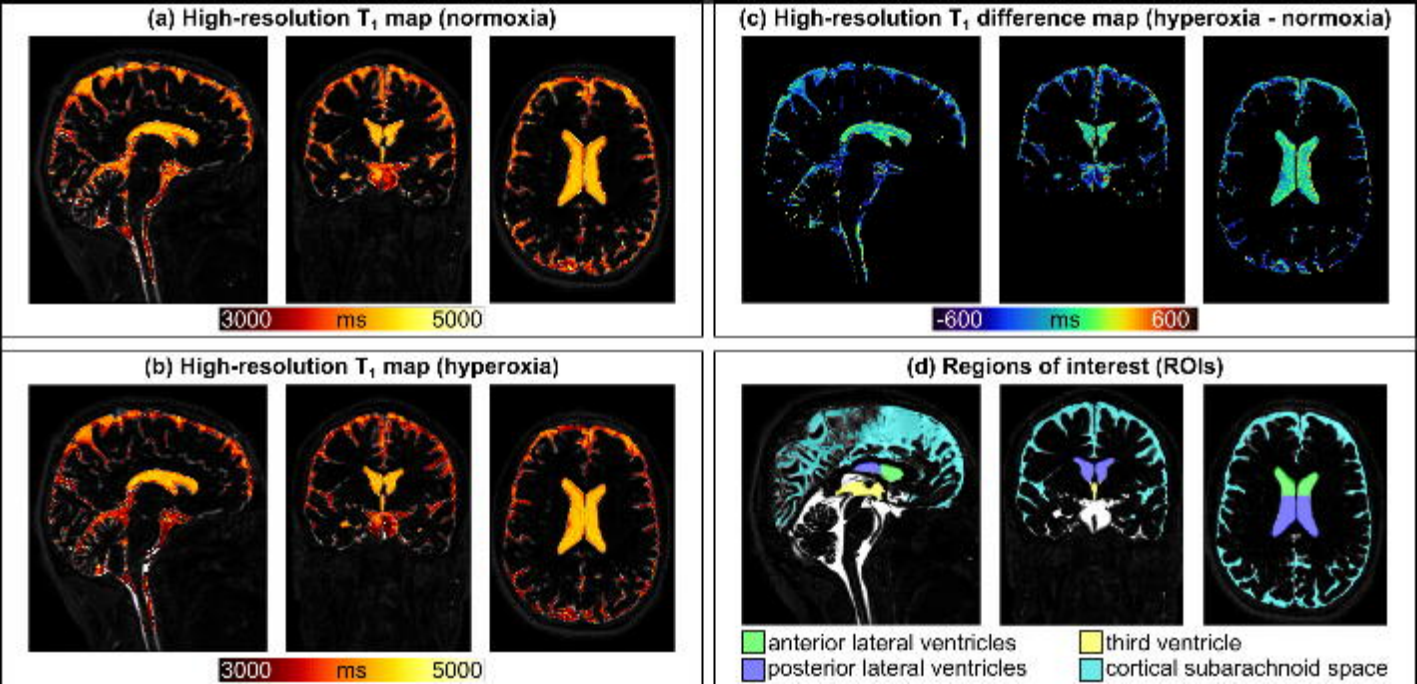
(a) High-resolution $T_1$ map (normoxia)
3000 ms 5000
(c) High-resolution $T_1$ difference map (hyperoxia - normoxia)
-600 ms 600
(b) High-resolution $T_1$ map (hyperoxia)
3000 ms 5000
(d) Regions of interest (ROIs)
anterior lateral ventricles
posterior lateral ventricles
third ventricle
cortical subarachnoid space

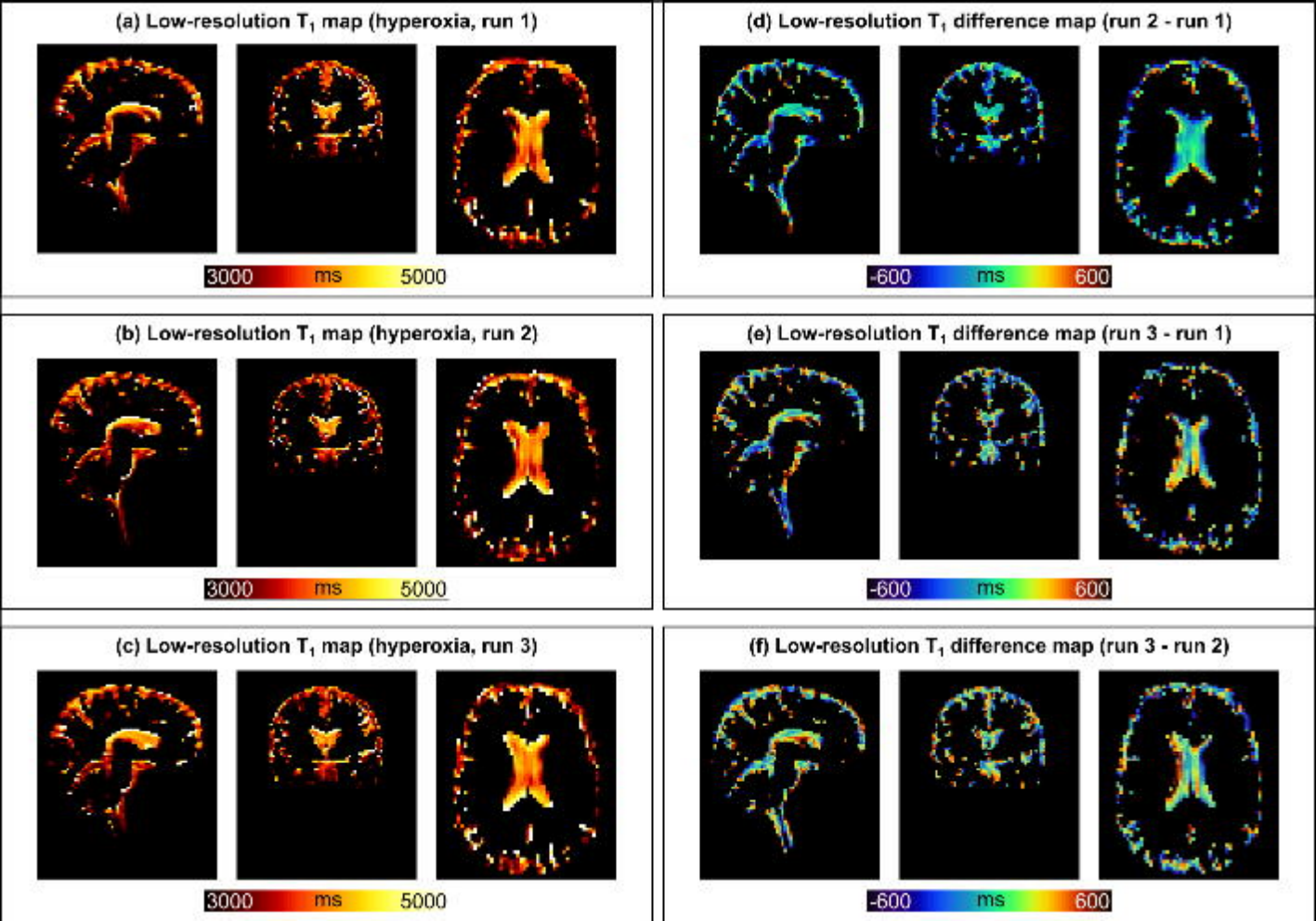
(a) Low-resolution T1 map (hyperoxia, run 1)
3000 ms 5000
(b) Low-resolution T1 map (hyperoxia, run 2)
3000 ms 5000
(c) Low-resolution T1 map (hyperoxia, run 3)
3000 ms 5000
(d) Low-resolution T1 difference map (run 2 - run 1)
-600 ms 600
(e) Low-resolution T1 difference map (run 3 - run 1)
-600 ms 600
(f) Low-resolution T1 difference map (run 3 - run 2)
-600 ms 600

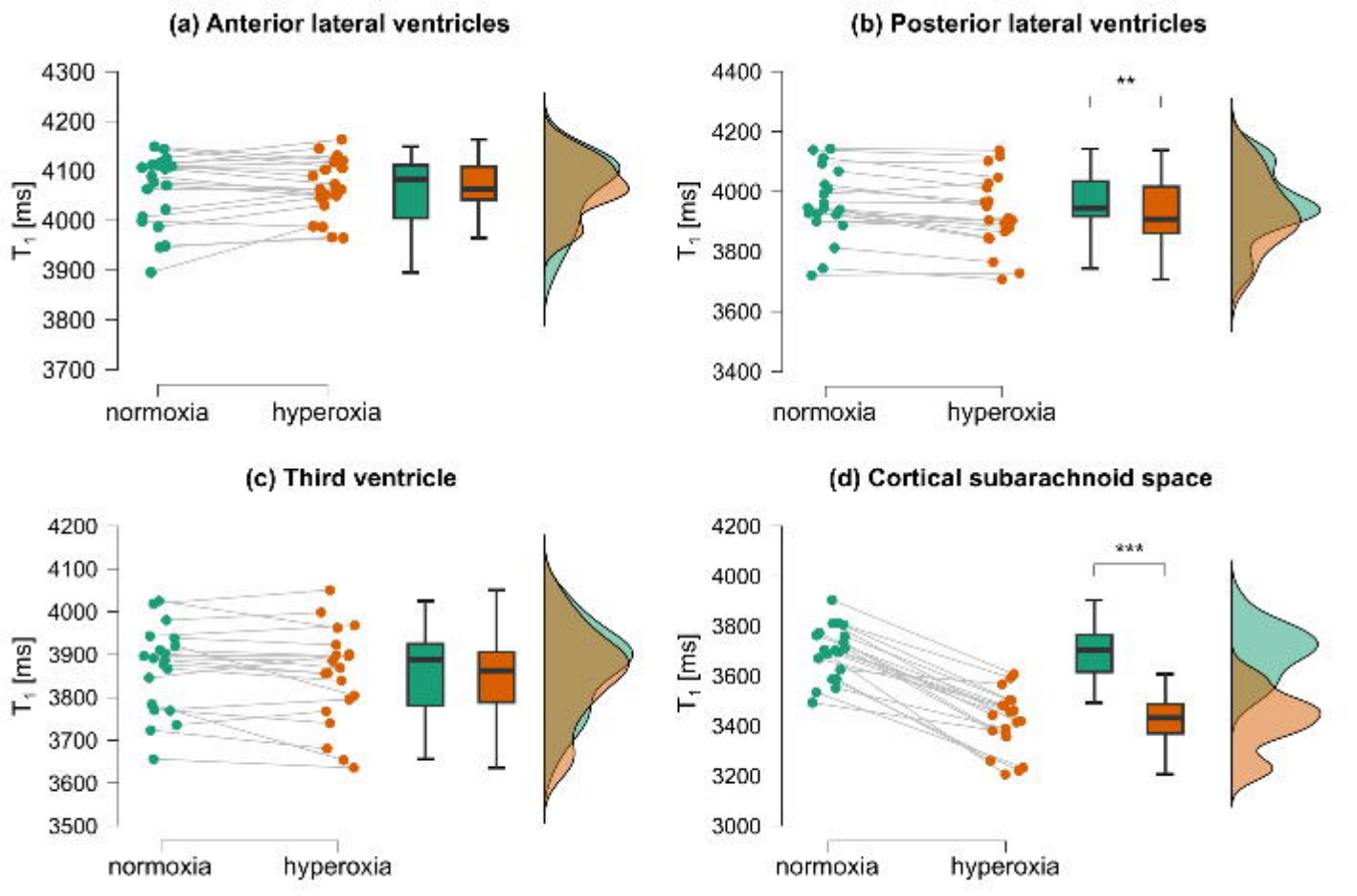
(a) Anterior lateral ventricles
4300
4200
4100
4000
3900
3800
3700
T1 [ms]
normoxia
hyperoxia
(b) Posterior lateral ventricles
**
4400
4200
4000
3800
3600
3400
T1 [ms]
normoxia
hyperoxia
(c) Third ventricle
4200
4100
4000
3900
3800
3700
3600
3500
T1 [ms]
normoxia
hyperoxia
(d) Cortical subarachnoid space
***
4200
4000
3800
3600
3400
3200
3000
T1 [ms]
normoxia
hyperoxia

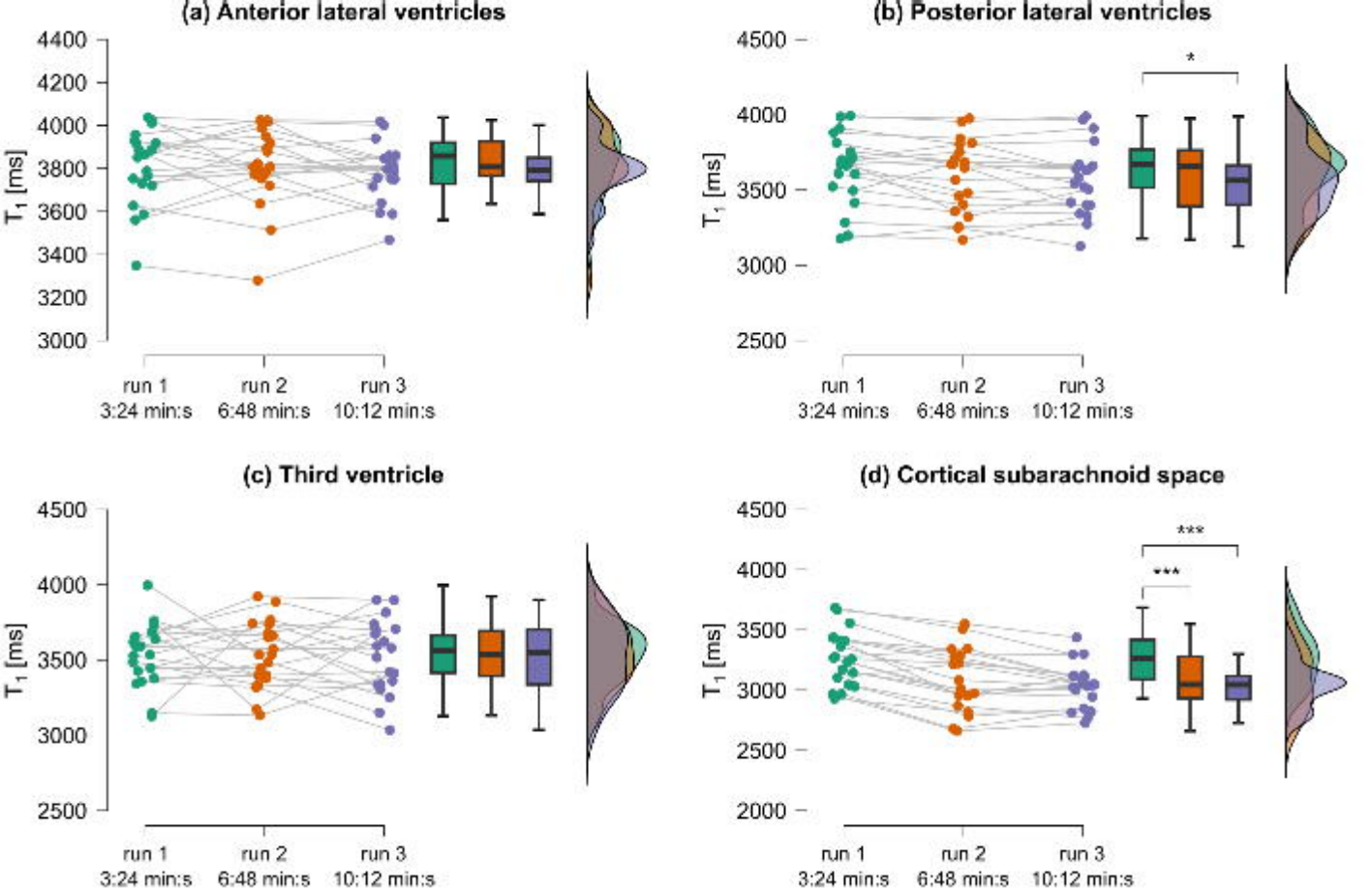
(a) Anterior lateral ventricles
(b) Posterior lateral ventricles
(c) Third ventricle
(d) Cortical subarachnoid space
T1 [ms]
run 1
3:24 min:s
run 2
6:48 min:s
run 3
10:12 min:s
*
***
***

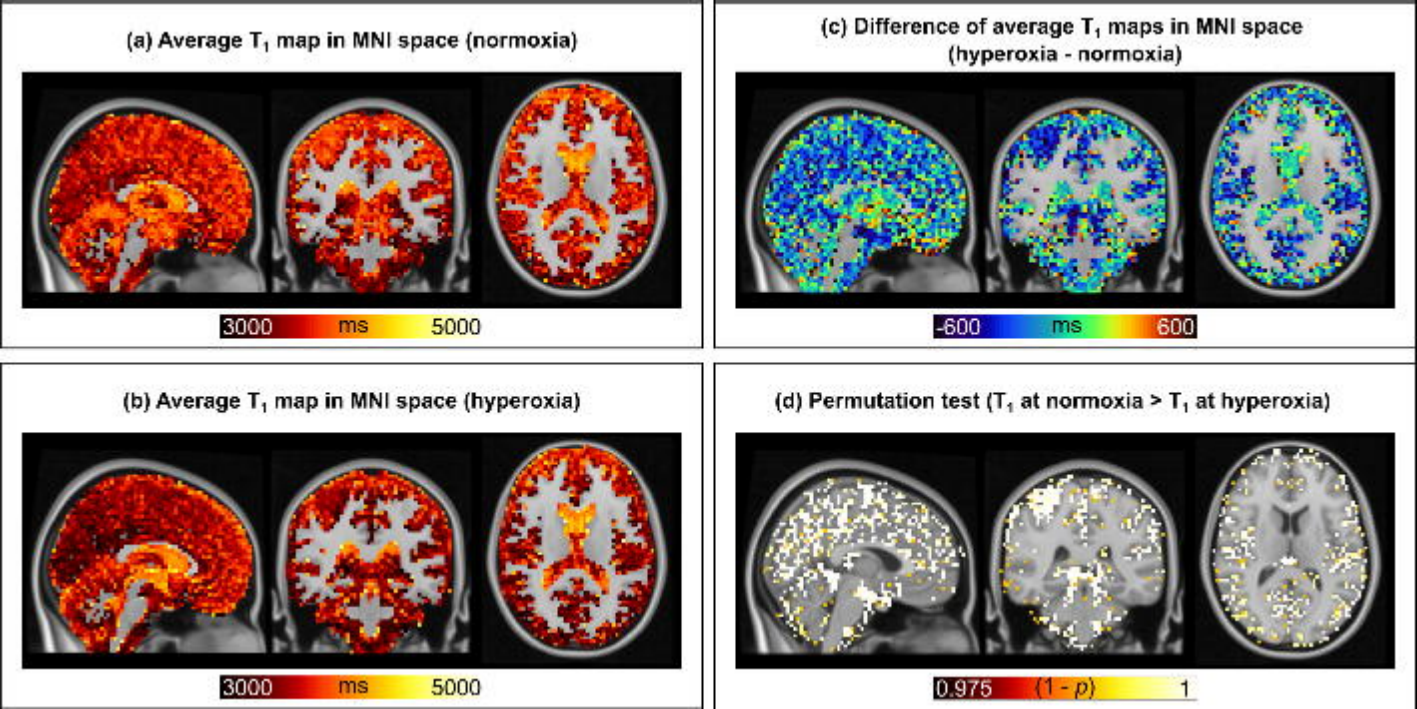
(a) Average $T_1$ map in MNI space (normoxia)
3000 ms 5000
(c) Difference of average $T_1$ maps in MNI space (hyperoxia - normoxia)
-600 ms 600
(b) Average $T_1$ map in MNI space (hyperoxia)
3000 ms 5000
(d) Permutation test ($T_1$ at normoxia > $T_1$ at hyperoxia)
0.975 (1 - p) 1